Multi-stage Deep Learning Artifact Reduction for Computed Tomography

Jiayang Shi, Daniël M. Pelt, K. Joost Batenburg

September 4, 2023

Abstract

In Computed Tomography (CT), an image of the interior structure of an object is computed from a set of acquired projection images. The quality of these reconstructed images is essential for accurate analysis, but this quality can be degraded by a variety of imaging artifacts. To improve reconstruction quality, the acquired projection images are often processed by a pipeline consisting of multiple artifact-removal steps applied in various image domains (e.g., outlier removal on projection images and denoising of reconstruction images). These artifact-removal methods exploit the fact that certain artifacts are easier to remove in a certain domain compared with other domains.

Recently, deep learning methods have shown promising results for artifact removal for CT images. However, most existing deep learning methods for CT are applied as a post-processing method after reconstruction. Therefore, artifacts that are relatively difficult to remove in the reconstruction domain may not be effectively removed by these methods. As an alternative, we propose a multi-stage deep learning method for artifact removal, in which neural networks are applied to several domains, similar to a classical CT processing pipeline. We show that the neural networks can be effectively trained in succession, resulting in easy-to-use and computationally efficient training. Experiments on both simulated and real-world experimental datasets show that our method is effective in reducing artifacts and superior to deep learning-based post-processing.

1   Introduction

CT is a non-invasive imaging technique that has become widely popular in various fields. CT allows for the analysis of the internal structure of objects in a non-invasive manner. Popular application fields of CT include medical imaging for disease diagnostics, industrial non-destructive testing, and security screening for parcel and luggage inspection [18]. CT systems used in those fields can differ significantly, as they must provide specific scanning capabilities required for the specific task. Despite these differences, CT systems typically follow a similar workflow for obtaining images of the object's interior structure. The typical workflow involves three sequential stages. First, the data is acquired as projection images, each of which encodes a directional X-ray view of the object. Second, the acquired projection images are converted to sinogram images. Finally, using the sinogram images, reconstruction images are computed, which display the internal structure of the object and are therefore suitable for further analysis.

The accuracy of CT analysis heavily relies on the quality of the reconstructed images. However, in many cases, the image quality can be insufficient for further analysis. These effects are particularly challenging in low-dose CT, which is widely used in modern CT systems to reduce radiation dose and scanning time. In low-dose CT, the acquired projection images typically contain significant amounts of noise, caused by the relatively low photon count received at each detector pixel. Noisy projection images result in high noise levels in the reconstructed images, hampering the detection of object features for further

1

analysis.

Reducing the noise in reconstructed CT images has been an active field of research for many years. Classical approaches of noise reduction include filtering of the reconstructed image [16], iterative reconstruction [27, 45], and Block-matching with 3D filtering (BM3D) [11]. Recently, deep-learning-based methods have become increasingly popular due to their superior noise reduction results over classical approaches. Many popular deep learning methods for CT noise reduction use a post-processing approach, in which a convolutional neural network (CNN) is applied to the final reconstruction images [8, 33, 54].

In addition to noise, a variety of artifacts can be introduced in the acquisition of projection images [5]. They propagate through the processing pipeline and result in artifacts in reconstruction images. For example, variations in detector response can cause ring-like artifacts to appear in reconstruction images [6, 35]. Similarly, single outliers captured by the detector can cause zingers [29], resulting in crossing-line artifacts in the reconstructed images. The key difference between noise and these other types of artifacts is that they are typically non-local in the reconstruction image. Non-local artifacts are challenging to reduce in reconstruction images by methods that exploit local image information, such as the popular post-processing deep learning methods [15].

In this paper, we present a deep learning method for artifact reduction in CT images that is specifically designed for reducing non-local artifacts in addition to noise. The idea of our approach is to follow a similar approach to existing classical methods for reducing such artifacts, in a multi-stage manner that spans across the different data domains.

Existing processing pipelines typically include a range of classical (i.e. non-learning) methods aimed at reducing artifacts that are non-local in the reconstruction image [3, 4, 6, 10, 13, 17, 23, 28, 29, 31, 32, 39, 42, 46–48, 50]. These methods aim to suppress the artifacts at an early stage in the processing pipeline. Examples are the reduction of zingers [13, 17, 29, 39], which can be carried out by detecting and filtering outliers in the projection images, and ring artifacts [3, 4, 6, 23, 28, 31, 32, 42, 46, 47, 50], which can be reduced by detecting and filtering lines in the sino-

gram images. Although these methods are effective and commonly used at experimental facilities, they have several disadvantages. First, they typically require the correct setting of several parameters to reduce artifacts properly, which are difficult to choose a priori. Second, the methods can introduce additional artifacts themselves, especially if the parameters were not set optimally. In contrast, in this paper we present a computationally efficient data-driven approach that can automatically learn the parameters for effective artifact reduction, without introducing additional artifacts further on in the pipeline.

Our approach is based on exploiting the fact that each artifact corresponds to particular stages of the processing pipeline where it can be naturally mitigated. To take advantage of this, we propose to use a sequence of three CNNs, each trained to target artifacts at a specific processing step. First, the projection images are processed by a CNN to reduce artifacts that are relatively easy to reduce in projection images. The sinogram image and the output of this first CNN are then processed by a second CNN operating in the sinogram domain. Finally, a third CNN is applied to the reconstruction images, in addition to the reconstructed outputs of the first and second CNNs, to produce the final artifact-reduced reconstruction image. To ensure computationally efficient training, we train the three CNNs independently in a sequential manner. We show that high-quality references for each stage, essential for training using supervised learning, can be obtained in several ways in practice, for example by scanning reference objects with a high-dose and/or a large number of projections. Details on obtaining reference data are discussed in Section 3.3.

Our method shares similarities with unrolled deep learning methods [1, 2] as both apply neural networks to different domains. Unrolled methods, typically applied in the sinogram and reconstruction domains, can implicitly learn to reduce certain artifacts. Nevertheless, they do not explicitly map sinograms to artifact-free sinograms, potentially limiting their artifact reduction capabilities. Additionally, unrolled methods involve multiple computationally costly tomographic operations both during training and application, leading to substantial computational costs

2

that can hinder their practical application. In contrast, the neural networks in our method can be trained and applied sequentially, avoiding the high computational costs of iteratively performing tomographic operations. This advantage allows for computationally efficient artifact reduction and easy use in practice.

This paper is organized as follows. Section 2 provides an overview of the related concepts and notation that underlie our motivation for the proposed method. In Section 3, we describe the details of our method, which involves using a series of CNNs to reduce artifacts at different stages of the processing pipeline, and describe ways of obtaining high-quality reference data for training. Section 4 covers the experimental design and implementation specifics. In Section 5, we present and analyze the experimental results. Section 6 is dedicated to discussing the implications and significance of our findings. Lastly, in Section 7, we conclude the paper by highlighting potential application areas for our method.

2   Notation and concepts

Different CT scanning configurations exist, such as parallel beam, circular cone-beam, and helical cone-beam. Our method is applicable for both parallel and cone-beam CT, and it works with circular and helical trajectories. In this work, we focus on the parallel and circular cone-beam CT.

In this section, we first provide a comprehensive overview of the CT pipeline that forms the basis of our method. We then define the general notation for CT artifacts that arise from the acquisition process and show how they propagate through the pipeline, leading to artifacts in the reconstructed images. Next, we discuss deep learning-based denoising methods for CT images and define their notations. Finally, we introduce and define the notations for classical artifact reduction operations that are performed at different steps of the pipeline. This foundation establishes the context and terminology for our proposed artifact reduction method.

2.1   CT pipeline

We present a model of a CT pipeline, illustrated in Figure 1, with three sequential steps. First, the CT system scans the object and acquires a series of projection images. Second, those projection images are rearranged into sinogram images. Finally, the reconstructed images are computed. While in cone-beam CT systems, the conversion from projection images to sinogram images is not necessary for reconstruction, we still include this step to reduce non-local artifacts on sinogram images, such as ring artifacts. Thus, our proposed pipeline is suitable for both parallel and cone-beam CT.

Given a detector with $M \times N$ pixels and N_θ scanning angles, the object is scanned along a trajectory, producing projection images $\mathbf{p} \in \mathbb{R}^{N_\theta \times M \times N}$. We first introduce the rearrange operation, denoted as $\mathcal{T}$, where

$$\mathcal{T} : \mathbb{R}^{N_\theta \times M \times N} \to \mathbb{R}^{M \times N_\theta \times N}. \qquad (1)$$

We define sinogram images as the rearranged projection images $\mathbf{s} \in \mathbb{R}^{M \times N_\theta \times N}$. In the reconstruction stage, reconstruction methods are applied to the sinogram images to compute the reconstructed images $\mathbf{r} \in \mathbb{R}^{Z \times Y \times X}$. The reconstruction operation is $\mathcal{R}$, where

$$\mathcal{R} : \mathbb{R}^{M \times N_\theta \times N} \to \mathbb{R}^{Z \times Y \times X}. \qquad (2)$$

The projection images $\mathbf{p}$, sinogram images $\mathbf{s}$, and reconstructed images $\mathbf{r}$ represent the same underlying object and are three data representations in the pipeline.

2.2   Artifacts

We focus on noise, ring, and zinger artifacts. For a general artifact introduced by the imaging process, we illustrate its propagation through the pipeline, leading to artifacts in the reconstructed images. Additionally, we provide schematic representations of the different artifacts in each pipeline stage to facilitate a better understanding of their characteristics.

Corrupted projections $\hat{\mathbf{p}} = \{\hat{\mathbf{x}}_1, ..., \hat{\mathbf{x}}_{N_\theta}\}$ consist of a series of corrupted projection images $\hat{\mathbf{x}}_i$, and are
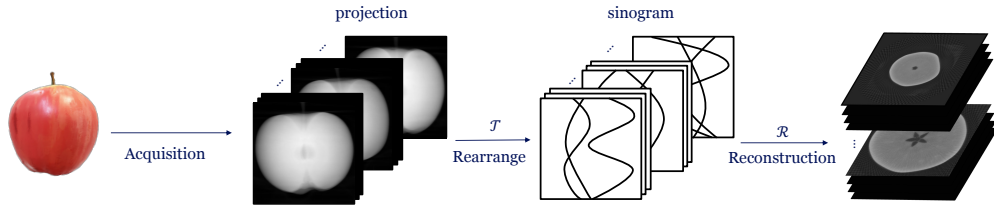
Figure 1: Schematic representation of a typical CT pipeline, consisting of three stages: projection, sinogram, and reconstruction stage.

a combination of the underlying clean projection images $\mathbf{p}$ and artifacts $\mathbf{n}$,

$$\hat{\mathbf{p}} = \mathbf{p} + \mathbf{n}. \qquad (3)$$

For example, $\mathbf{n}$ can contain noise, offsets of pixel values that cause ring artifacts, and/or outliers that cause zinger artifacts. In a scenario where no artifact removal steps are included in the CT pipeline and, for illustration, we assume a linear reconstruction operation $\mathcal{R}_{lin}$, the resulting reconstruction images would be expressed as $\hat{\mathbf{r}}$:

$$\hat{\mathbf{r}} = \mathcal{R}_{lin}\left(\mathcal{T}\left(\hat{\mathbf{p}}\right)\right) = \mathcal{R}_{lin}\left(\mathcal{T}\left(\mathbf{p}\right)\right) + \mathcal{R}_{lin}\left(\mathcal{T}\left(\mathbf{n}\right)\right). \qquad (4)$$

Here, $\mathcal{R}_{lin}\left(\mathcal{T}\left(\mathbf{p}\right)\right)$ represents the ideal artifact-free reconstruction image, and $\mathcal{R}_{lin}\left(\mathcal{T}\left(\mathbf{n}\right)\right)$ represents the artifacts originating from artifact term $\mathbf{n}$ in corrupted projection images. In this manner, artifacts that occur during acquisition are passed through the pipeline and become artifacts in the reconstructed images. In the following, we describe three common artifact types encountered in (high-energy) CT systems. Existing methods for reducing artifacts are discussed in Section 2.4.

2.2.1 Noise

Poisson noise is a common artifact in CT, arising from insufficient photon counts at the detector [5]. Low-dose CT can suffer from strong noise artifacts due to fewer photons captured by the detector pixels. Poisson noise is introduced during acquisition and presents as local disruptions in projection images. It corresponds to a local perturbation in all stages of the CT pipeline, as illustrated in Figure 2.
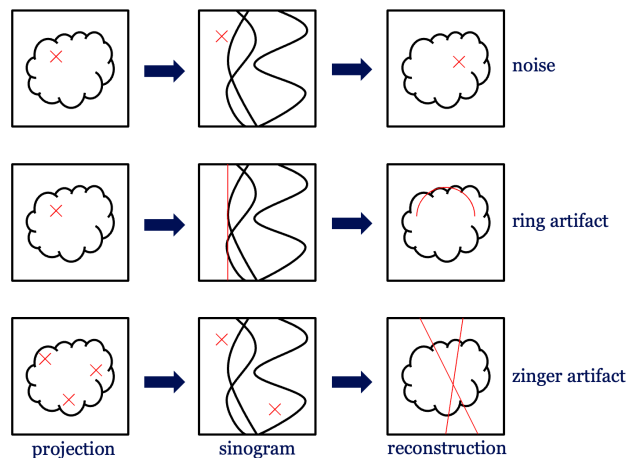
Figure 2: Representations of noise, ring, and zinger artifact in projection, sinogram, and reconstruction stages. Red patterns are schematic illustrations of distortions. Noise is a local artifact in images of all stages. A distorted pixel value in the projection images becomes a line in the sinogram, resulting in a ring artifact in the reconstructed image. Extremely high pixel values remain as high-value spots in the sinogram and cause crossing lines in the reconstructed image as zinger artifacts.

4

2.2.2 Ring Artifact

Ring artifacts arise from systematic detector errors, such as miscalibrated or defective elements in the detector. For example, as demonstrated in Figure 2, a detector element may record its value with an additive offset applied to the actual data [5, 35]. Consistent detector offsets in the projection images translate to straight lines in sinogram images and become ring-like artifacts in the reconstructed images.

2.2.3 Zinger Artifact

Zinger artifacts often appear in high-energy CT, such as synchrotron CT. It is caused by extremely high-value spots in projection images because the detector occasionally records high-energy photons [29]. These erroneously high values don't correspond to the scanned object. Since these spots' occurrence is stochastic among projections, they appear as prominent local spots in sinograms, as shown in Figure 2. After reconstruction, the local artifacts become crossing streaks in the reconstructed images.

2.3 Denoising with Deep Learning

Deep learning methods have shown promising results in CT image denoising. One popular approach for denoising low-dose CT is using a CNN as a post-processing step on reconstructed images [8, 33, 54]. To gain such denoising ability, the CNN is trained in a supervised manner, learning the mapping from low-quality reconstructed images to their corresponding high-quality ones. We explain denoising with a CNN on reconstructed images in the following.

We use the notation f_θ to represent the CNN, where θ corresponds to the network's trainable parameters. In post-processing deep learning for CT images, the CNN is applied directly to the corrupted reconstruction image $\hat{\mathbf{r}}$ to produce a denoised reconstruction image $\mathbf{r}^{\mathrm{PP}}$:

$$\mathbf{r}^{\mathrm{PP}} = f_\theta(\hat{\mathbf{r}}) \qquad (5)$$

Note that in this paper we will focus on CNNs that process two-dimensional images using two-dimensional convolutional operations, as these are computationally more efficient than three-dimensional CNNs. Since CT images are typically large, i.e. often larger than 1000^3 pixels, 3D CNNs can have prohibitive computational costs. The notation in Equation 5 represents applying the 2D CNN f_θ to each of the Z slices of $\hat{\mathbf{r}}$ separately, and collecting the Z output images in $\mathbf{r}^{\mathrm{PP}}$.

To determine the parameters θ of the CNN f_θ such that $\mathbf{r}^{\mathrm{PP}}$ approximates an artifact-free reconstruction, *supervised learning* is often used. In supervised learning, we assume that for a set of N^t corrupted reconstructions $\hat{\mathbf{r}}_i$ we have corresponding high-quality reference reconstructions $\mathbf{r}_i^{\mathrm{HQ}}$ available, resulting in a training set $X = \{(\hat{\mathbf{r}}_1, \mathbf{r}_1^{\mathrm{HQ}}), \ldots, (\hat{\mathbf{r}}_{N^t}, \mathbf{r}_{N^t}^{\mathrm{HQ}})\}$. High-quality reconstructions can be obtained in various ways, for example by scanning with a high radiation dose, acquiring a large number of projection images, or applying advanced reconstruction techniques for a set of reference objects. Given the training set X, suitable parameters for the post-processing CNN can be found by minimizing the following objective function:

$$\theta^* = \arg\min_\theta \sum_{i=1}^{N^t} L\left(f_\theta(\hat{\mathbf{r}}_i), \mathbf{r}_i^{\mathrm{HQ}}\right), \qquad (6)$$

where L is a loss function measuring the difference between the CNN output and the reference image.

Post-processing CNN methods have proven effective in reducing noise from CT images in a wide variety of applications. However, CNNs typically learn to exploit local information due to their use of small convolution kernels, even when their depth allows for large receptive fields. Therefore, we expect post-processing deep learning methods to be less effective for artifacts that are non-local in the reconstruction domain than for local artifacts. In Figure 3, results are shown for an experiment to test this hypothesis. The results show that the post-processing deep learning-based methods indeed perform well for noise reduction, but yield suboptimal results for non-local ring and zinger artifacts in addition to noise. This observation is the main motivation for developing the multi-stage method presented in this paper.
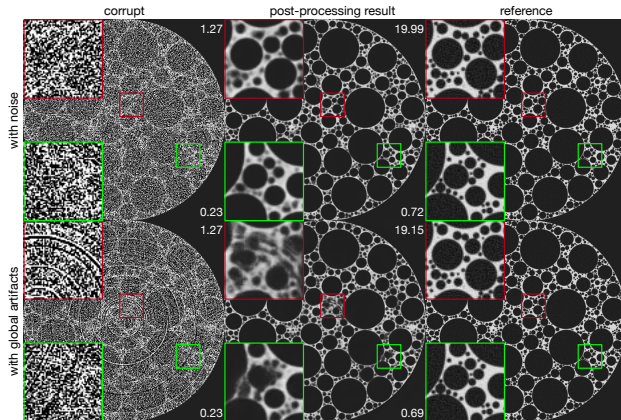
Figure 3: Comparison of deep learning-based post-processing performance on reconstructed images affected by noise and non-local artifacts. The red and green insets show enlarged views of the affected areas. PSNR and SSIM values are provided in the top-right and lower-right corners, respectively.

2.4 Classical Artifact Reduction Methods

In practice, classical (i.e. non-learning) artifact reduction methods are typically performed at different stages of the CT pipeline. Table 2.4 provides an overview of representative methods for reducing noise, ring, and zinger artifacts, and indicates the stages in the pipeline where they are applied. Ring artifact reduction is typically performed at the sinogram stage, while zinger artifact reduction is often applied to projections. On the other hand, denoising techniques are commonly used to process reconstructed images directly. To describe the various artifact reduction methods, we define the operations $\mathbf{A}_p$, $\mathbf{A}_s$, and $\mathbf{A}_r$ to denote the artifact reduction operations for projection, sinogram, and reconstructed images, respectively. In a pipeline that includes such methods, the reconstruction image $\mathbf{r}^{\mathrm{PL}}$ is computed by applying the methods at each stage:

$$\mathbf{r}^{\mathrm{PL}} = \mathbf{A}_r \left(\mathcal{R} \left(\mathbf{A}_s \left(\mathcal{T} \left(\mathbf{A}_p \left(\hat{\mathbf{p}} \right) \right) \right) \right) \right). \tag{7}$$

We introduce some classical methods for reducing noise, ring, and zinger artifacts that fit as $\mathbf{A}_p$, $\mathbf{A}_s$, and $\mathbf{A}_r$ in the pipeline. Classical denoising methods, often post-processing based, can reduce noise by calculating the pixel value from its neighbors, like median or Wiener filtering. Total Variation (TV)-based regularization methods [41] reduce noise iteratively under the local smoothness assumption. BM3D is based on the similarity of patches within an image [11]. These classical denoising methods can be mathematically expressed as $\mathbf{A}_r$ in Equation 7, since they are applied to reconstructed images. Often, noise reduction is performed (either explicitly or implicitly) by the reconstruction method $\mathcal{R}$ as well.

Ring artifacts, which appear as straight lines in sinograms, are often reduced by filtering these lines. Methods like [4,6,23,31] reduce the ring artifact by filtering the straight lines in the sinogram stage. Some methods [7,44] transform reconstructed images into the polar coordinate system, transforming rings into straight lines for line detection-based approaches. The common ring artifact reduction method that acts on sinogram images can be expressed as $\mathbf{A}_s$ in Equation 7. Zinger artifacts are often reduced in the projection images by filtering. For example, Tomopy [17] provides a zinger reduction function using median filters. The operation on projection images can be expressed as $\mathbf{A}_p$ in Equation 7.

3 Algorithm

In this section, we present our proposed multi-stage artifact reduction method and its motivation. We then provide a detailed description of the method, along with the training procedure of the CNNs and ways to obtain high-quality reference data for training. Finally, we discuss the key design choices that make our method computationally efficient.

3.1 Motivation for Multi-stage Artifact reduction

In the context of the CT pipeline described in Equation 7, deep learning-based denoising methods can be viewed as using a CNN f_θ to act as $\mathbf{A}_r$. However, for reconstructed images corrupted by globally distributed artifacts in addition to noise, post-

6

Table 1: Overview of artifact reduction methods at different stages of the CT pipeline.

Artifact	Projection	Sinogram	Reconstruction
Noise		$[14, 21, 25, 51]$	$[9, 20, 26, 27, 33, 37, 38, 43, 53, 55, 56]$
Ring	$[10, 48]$	$[3, 4, 6, 23, 28, 31, 32, 42, 46, 47, 50]$	$[7, 22, 30, 32, 44, 52, 57]$
Zinger	$[13, 17, 29, 39]$		$[22]$

processing can be insufficient, as shown in Figure 3. Classical methods reduce such artifacts effectively by processing the projection and sinogram data before reconstruction in the pipeline. This inspires the use of neural networks to replace $\mathbf{A}_p$ and $\mathbf{A}_s$ in addition to only replacing $\mathbf{A}_r$. In this way, the advantage of a classical CT pipeline is maintained, as some artifacts are easier to remove in projection or sinogram images than in reconstruction images. Compared with classical methods, using neural networks has the advantage that they can be optimized to each problem setting in a data-driven way, remove the need for setting sensitive parameters correctly, and ensure computational efficiency during the inference phase.

3.2 Multi-stage Artifact reduction

Our data-driven method, shown schematically in Figure 4, employs three CNNs serving as $\mathbf{A}_p$, $\mathbf{A}_s$, and $\mathbf{A}_r$ in Equation 7. Each stage employs a distinct neural network to process the projection, sinogram, and reconstruction data sequentially. The processed data from the previous stages are fed into each subsequent stage, improving the artifact reduction performance. The three CNNs are trained independently in a sequential manner, ensuring computationally efficiency during training.

In the first stage, we use a CNN $f_{\theta_p}^p$ to act as $\mathbf{A}_p$ for processing projection images in the Equation 7. We obtain processed projections $\mathbf{p}^*$ by applying $f_{\theta_p}^p$ on the corrupted projections $\hat{\mathbf{p}}$,

$$\mathbf{p}^* = f_{\theta_p}^p(\hat{\mathbf{p}}). \qquad (8)$$

As in Equation 5, the notation represents applying the 2D CNN $f_{\theta_p}^p$ to each of the N_θ projections of $\hat{\mathbf{p}}$, and collecting the N_θ output images in $\mathbf{p}^*$.
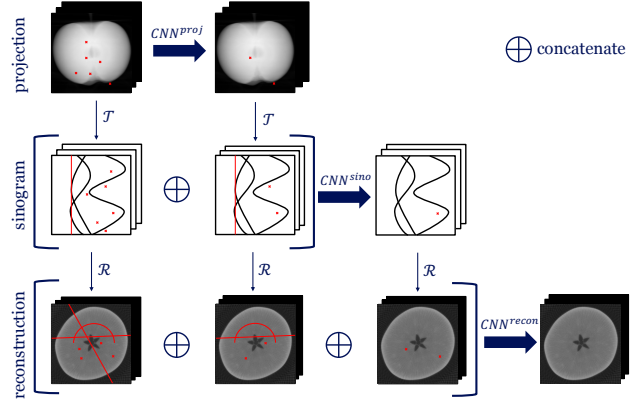
Figure 4: Our proposed multi-stage artifact reduction method. Red patterns are schematic illustrations of distortions and their resulting artifacts.

In the second stage, we use another CNN $f_{\theta_s}^s$ as $\mathbf{A}_s$ to process sinogram images in Equation 7. $f_{\theta_s}^s$ takes both corrupted sinograms $\mathcal{T}(\hat{\mathbf{p}})$ and the processed projections $\mathcal{T}(\mathbf{p}^*)$ as input, and output processed sinograms $\mathbf{s}^*$,

$$\mathbf{s}^* = f_{\theta_s}^s(\mathcal{T}(\hat{\mathbf{p}}), \mathcal{T}(\mathbf{p}^*)). \qquad (9)$$

As above, the notation represents applying the 2D CNN $f_{\theta_s}^s$ to each of the M sinograms of $\hat{\mathbf{p}}$ and $\mathcal{T}(\mathbf{p}^*)$, and collecting the M output images in $\mathbf{s}^*$. In the final stage, we use the third CNN $f_{\theta_r}^r$ to act as $\mathbf{A}_r$ for the reconstructed images in Equation 7. The input to the network consists of corrupted reconstructions $\mathcal{R}(\mathcal{T}(\hat{\mathbf{p}}))$, reconstructions of the output of the first stage $\mathcal{R}(\mathcal{T}(\mathbf{p}^*))$, and reconstructions of the output of the second stage $\mathcal{R}(\mathbf{s}^*)$:

$$\mathbf{r}^* = f_{\theta_r}^r(\mathcal{R}(\mathcal{T}(\hat{\mathbf{p}})), \mathcal{R}(\mathcal{T}(\mathbf{p}^*)), \mathcal{R}(\mathbf{s}^*)) \qquad (10)$$

As above, the notation represents applying the 2D

CNN $f_{\theta_r}^r$ to each of the Z slices of $\mathcal{R}\left(\mathcal{T}\left(\hat{\mathbf{p}}\right)\right)$, $\mathcal{R}\left(\mathcal{T}\left(\mathbf{p}^*\right)\right)$, and $\mathcal{R}\left(\mathbf{s}^*\right)$, and collecting the Z output images in $\mathbf{r}^*$. Our method is summarized in Algorithm 1.

Algorithm 1 Inference method

Input: low-quality projection images $\hat{\mathbf{p}}$, reconstruction method $\mathcal{R}$, trained networks $f_{\theta_p}^p$, $f_{\theta_s}^s$, and $f_{\theta_r}^r$.

Output: reconstruction images with reduced artifacts $\mathbf{r}^*$

1: **procedure** INFERENCE
2:      Apply $f_{\theta_p}^p$ to $\hat{\mathbf{p}}$ to obtain projection images $\mathbf{p}^* = f_{\theta_p}^p(\hat{\mathbf{p}})$.
3:      Rearrange the low-quality projection images $\hat{\mathbf{p}}$ and the output of the first CNN $\mathbf{p}^*$ to obtain sinogram images $\mathcal{T}\left(\hat{\mathbf{p}}\right)$ and $\mathcal{T}\left(\mathbf{p}^*\right)$
4:      Apply $f_{\theta_s}^s$ to the two sets of sinogram images to obtain output sinogram images $\mathbf{s}^* = f_{\theta_s}^s\left(\mathcal{T}\left(\hat{\mathbf{p}}\right), \mathcal{T}\left(\mathbf{p}^*\right)\right)$
5:      Reconstruct the low-quality projection images and the outputs of both CNNs to obtain $\mathcal{R}\left(\mathcal{T}\left(\hat{\mathbf{p}}\right)\right), \mathcal{R}\left(\mathcal{T}\left(\mathbf{p}^*\right)\right), \mathcal{R}\left(\mathbf{s}^*\right)$
6:      Apply $f_{\theta_r}^r$ to the three sets of reconstruction images from the previous step to obtain output reconstruction images $\mathbf{r}^* = f_{\theta_r}^r\left(\mathcal{R}\left(\mathcal{T}\left(\hat{\mathbf{p}}\right)\right), \mathcal{R}\left(\mathcal{T}\left(\mathbf{p}^*\right)\right), \mathcal{R}\left(\mathbf{s}^*\right)\right)$
7: **end procedure**

3.3   Training Procedure

It is possible to view the multi-stage method described in Algorithm 1 as one large neural network that takes the corrupted projections and produces a reconstruction, with a set of learnable parameters $\Theta = \{\theta_p, \theta_s, \theta_r\}$. Any training approach suitable for such mappings, including the training approaches commonly used for post-processing deep learning methods, would be, at least in principle, applicable to find suitable values for Θ. However, even though the neural networks used in our approach are 2D, the fact that the method includes rearrange operations $\mathcal{T}$ and reconstruction operations $\mathcal{R}$ necessitates that such end-to-end training approaches have

to be performed in 3D. As explained above, the large size of typical CT problems makes such 3D training prohibitively computationally expensive. As an alternative, we propose a computationally efficient way of training the three CNNs separately in a sequential manner, ensuring practical applicability.

In the following, we will describe our proposed training procedure using a supervised learning approach, although other learning approaches such as self-supervised learning are possible as well. For the supervised training, high-quality reference projections, sinograms, and reconstructions are required. These high-quality references can be obtained in various ways, depending on the practical use case. One possibility is to scan the reference objects with a high dose and a large number of projections. In this case, reference reconstructions can be obtained by reconstructing the acquired high-quality data. If the set of projection angles of the low-quality scan is included in the set of projection angles of the high-quality scan, high-quality projections can be obtained by selecting the matching angles. If the projection angles do not match, one possibility is to simulate projections of high-quality reconstructions for the correct low-quality angles, for example using the ASTRA toolbox [49]. An alternative to high-dose reference scans is to create reconstructions with reduced artifacts for the reference objects by using advanced experimental setups that suppress artifacts [35, 58], and/or use sophisticated processing techniques with carefully chosen parameter settings. Afterward, projections from high-quality reconstruction can be simulated to obtain high-quality projections and sinograms.

We start by training CNN $f_{\theta_p}^p$ to find suitable parameters θ_p. Similar to the supervised learning described in Section 2.3, we assume that that for a set of N^t scanned objects with corrupted projections $\hat{\mathbf{p}}_i$ we have corresponding high-quality reference projections $\mathbf{p}_i^{\mathrm{HQ}}$ available, resulting in a training set $X^p = \{(\hat{\mathbf{p}}_1, \mathbf{p}_1^{\mathrm{HQ}}), \ldots, (\hat{\mathbf{p}}_{N^t}, \mathbf{p}_{N^t}^{\mathrm{HQ}})\}$. Given the training set X^p, suitable parameters for $f_{\theta_p}^p$ can be found

by minimizing the following objective function:

$$\theta_p^* = \arg\min_{\theta_p} \sum_{i=1}^{N^t} L^p \left(f_{\theta_p}^p(\hat{\mathbf{p}}_i), \mathbf{p}_i^{\mathrm{HQ}} \right) \qquad (11)$$

After training $f_{\theta_p}^p$, we continue by training the CNN $f_{\theta_s}^s$ that acts in the sinogram domain. Similar to above, we assume that for the same set of N^t scanned objects, we have pairs of corrupted sinograms $\hat{\mathbf{s}}_i = \mathcal{T}(\hat{\mathbf{p}}_i)$ and corresponding high-quality reference sinograms $\mathbf{s}_i^{\mathrm{HQ}}$ available. Note that in this case, it could happen that the high-quality sinograms include more projection angles, i.e. have more rows, than the corrupted sinograms. In this case, we upsample the corrupted sinograms to match the number of rows before using them as input to the neural networks. For all N^t reference objects, we also compute projections $\mathbf{p}_i^* = f_{\theta_p^*}^p(\hat{\mathbf{p}}_i)$ corresponding to the output of the first trained network. Given the training set, suitable parameters for $f_{\theta_s}^s$ can be found by minimizing the following objective function:

$$\theta_s^* = \arg\min_{\theta_s} \sum_{i=1}^{N^t} L^s \left(f_{\theta_s}^s(\hat{\mathbf{s}}_i, \mathcal{T}(\mathbf{p}_i^*)), \mathbf{s}_i^{\mathrm{HQ}} \right) \qquad (12)$$

Finally, we train the CNN $f_{\theta_r}^r$ that acts in the reconstruction domain. Similar to above, we assume that for the same set of N^t scanned objects, we have pairs of corrupted reconstructions $\hat{\mathbf{r}}_i = \mathcal{R}(\hat{\mathbf{s}}_i)$ and corresponding high-quality reference reconstructions $\mathbf{r}_i^{\mathrm{HQ}}$ available. For all N^t reference objects, we also compute sinograms $\mathbf{s}_i^* = f_{\theta_s^*}^s(\hat{\mathbf{s}}_i, \mathcal{T}(\mathbf{p}_i^*))$ corresponding to the output of the second trained network. Given the training set, suitable parameters for $f_{\theta_r}^r$ can be found by minimizing the following objective function:

$$\theta_r^* = \arg\min_{\theta_r} \sum_{i=1}^{N^t} L^r \left(f_{\theta_r}^r(\hat{\mathbf{r}}_i, \mathcal{R}(\mathcal{T}(\mathbf{p}_i^*)), \mathcal{R}(\mathbf{s}_i^*)), \mathbf{r}_i^{\mathrm{HQ}} \right)$$
$$(13)$$

The training approach is summarized in Algorithm 2.

4 Experiments

In this section, we explain the purpose of our experiments and describe the datasets, on which we con-

---

Algorithm 2 Training procedure

Input: low-quality projection images $\hat{\mathbf{p}}_i$ and high-quality projections $\mathbf{p}_i^{\mathrm{HQ}}$, sinograms $\mathbf{s}_i^{\mathrm{HQ}}$, and reconstructions $\mathbf{r}_i^{\mathrm{HQ}}$ for a set of N^t reference objects. Loss functions L^p, L^s, and L^r.

Output: weights of CNNs: θ_p^*, θ_s^*, θ_r^*.

1: **procedure** TRAINING
2:     Train in the projection domain to obtain $\theta_p^* = \arg\min_{\theta_p} \sum_{i=1}^{N^t} L^p \left(f_{\theta_p}^p(\hat{\mathbf{p}}_i), \mathbf{p}_i^{\mathrm{HQ}} \right)$.
3:     Compute projections $\mathbf{p}_i^* = f_{\theta_p^*}^p(\hat{\mathbf{p}}_i)$ corresponding to the output of the first trained network.
4:     Train in the sinogram domain to obtain $\theta_s^* = \arg\min_{\theta_s} \sum_{i=1}^{N^t} L^s \left(f_{\theta_s}^s(\hat{\mathbf{s}}_i, \mathcal{T}(\mathbf{p}_i^*)), \mathbf{s}_i^{\mathrm{HQ}} \right)$.
5:     Compute sinograms $\mathbf{s}_i^* = f_{\theta_s^*}^s(\hat{\mathbf{s}}_i, \mathcal{T}(\mathbf{p}_i^*))$ corresponding to the output of the second trained network.
6:     Train in the reconstruction domain to obtain $\theta_r^* = \arg\min_{\theta_r} \sum_{i=1}^{N^t} L^r \left(f_{\theta_r}^r(\hat{\mathbf{r}}_i, \mathcal{R}(\mathcal{T}(\mathbf{p}_i^*)), \mathcal{R}(\mathbf{s}_i^*)), \mathbf{r}_i^{\mathrm{HQ}} \right)$.
7: **end procedure**

duct those experiments. In addition, we describe our implementation details and introduce the metrics we used to asses those experiments.

4.1 Experiment Design

We conducted four tailored experiments to validate our method. First, we used a simulated dataset to compare our approach against a deep learning post-processing technique. Second, we contrasted it with classical artifact reduction tools followed by deep learning-based post-processing, notably the outlier removal and Fourier-Wavelet ring removal from To-moPy [31], underscoring challenges in optimal parameter selection for classical techniques. Third, we integrated our solution into a standard cone-beam CT pipeline, examining the effect of different source-object distances (SODs) and comparing efficiency between cone-beam and parallel-beam CT. Fourth, using an experimental CT dataset, we assessed our method's real-world robustness, emphasizing its superiority over deep learning post-processing and its potential for seamless integration into existing CT pipelines.

4.2 Datasets

4.2.1 Simulated data

We generated simulated cylinder foam phantoms using the package `foam_ct_phantom` [34]. For each experimental setup, two phantoms were generated: one for training and one for testing purposes. Each phantom consisted of 100000 non-overlapping bubbles of varying sizes randomly distributed within a cylinder. While the training and testing phantoms contained the same number of bubbles, they were generated with different spacing configurations. Projection images of 512×512 pixels were simulated for 1024 angles equally distributed in $180°$ with a parallel beam geometry. For the cone-beam experiment a similar setup was used, with the detector positioned at the center of the foam phantom cylinder to achieve an ideal object-detector distance of zero and the source-object distance varied to produce different cone angles in the experiment. To simulate low-dose pro-

jections, the generated projection images were corrupted with Poisson noise in the same way as described in [34], i.e. through converting projection data to raw photon counts. For more noise generation details, we refer to [34]. In this approach, the noise level is controlled by two parameters: the average absorption γ and the incident photon count I_0. In our experiments, we set the average absorption γ such that roughly half of the photons are absorbed by the object and vary the photon count I_0 to generate different noise levels.

We simulate ring and zinger artifacts based on their respective occurrence mechanisms. Ring artifacts were simulated by introducing fixed deviations to a randomly selected subset of detector pixels, mimicking the scenario where certain elements of the detector recorded values with systematic errors. The deviations, denoted as $\mathbf{d}_{\mathrm{ring}} \in \mathbb{R}^{M \times N}$, were determined based on the percentage of affected pixels P_{ring} and standard deviation σ_{ring}:

$$\mathbf{d}_{\mathrm{ring}} = \mathbf{M}\left(P_{\mathrm{ring}}\right) \mathcal{N}\left(\mathbf{0},\, \sigma_{\mathrm{ring}}^2 \mathbf{I}\right), \qquad (14)$$

where $\mathbf{M}\left(P_{\mathrm{ring}}\right)$ represents a fixed mask with P_{ring} percentage of pixels set to one and the rest set to zero. The corrupted projections $\hat{\mathbf{p}} = \{\hat{\mathbf{x}}_1, ..., \hat{\mathbf{x}}_{N_\theta}\}$ were obtained by adding $\mathbf{d}_{\mathrm{ring}}$ to each projection image $\mathbf{x}_i$:

$$\hat{\mathbf{x}}_i = \mathbf{x}_i + \mathbf{d}_{\mathrm{ring}}. \qquad (15)$$

The parameter P_{ring} controls the amount of ring-like artifacts in a single reconstructed slice, while a larger σ_{ring} results in higher pixel values of occurred rings. In the following, σ_{ring} is fixed at 0.005, and P_{ring} is adjusted to change the severity.

To simulate zinger artifacts, we replaced a small subset of randomly chosen pixel values with excessively high values in certain projection images. The excessively high values were aimed to simulate the highest values that a detector can receive. The severity of the zinger artifact is controlled using three parameters: the percentage of affected projections P_{proj}, the percentage of affected pixels in the affected projection P_{zinger}, and the excessively high value v. We set P_{proj} at 10%, indicating that 10% of the total number of projection images were affected and fixed v at 5. We use P_{zinger} to vary the severity of
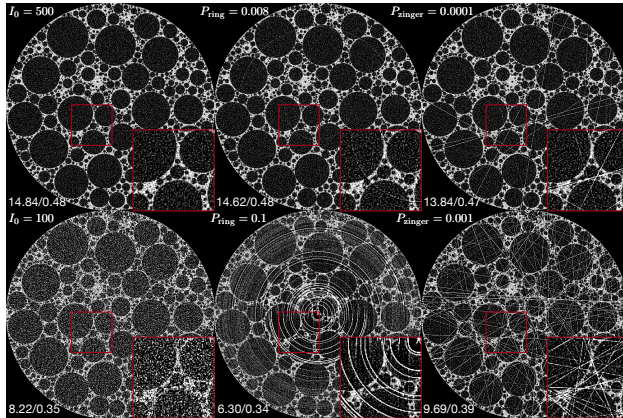
Figure 5: Example image with various levels of artifacts on a simulated foam phantom dataset. The artifacts, including noise, ring artifacts, and zinger artifacts, were generated by varying the parameters I_0, P_{ring}, and P_{zinger}, respectively. The PSNR and SSIM metrics with respect to the ground truth image are provided for each reconstructed image, displayed in the bottom left.

the zinger artifact, where increasing P_{zinger} leads to more streaks in every reconstructed slice.

In addition to noise and ring artifacts, the quality of the reconstructed image was further degraded in low-quality data by using only 256 projection images, while high-quality data used all 1024 projection images. The reconstruction images were computed using the GPU-accelerated FBP and FDK implementations of the ASTRA toolbox [49]. The reconstructed phantom consisted of $512 \times 512 \times 512$ voxels, and a circular filter from TomoPy [17] was applied to remove the corners of each slice. Figure 5 shows examples of the simulated foam phantom with artifacts of different severity levels, showing that reducing I_0 leads to more noise and increasing P_{ring} and P_{zinger} results in more severe ring and zinger artifacts, respectively, in the reconstructed images.

4.2.2 Experimental data

To validate our method, we utilized a real-world experimental dataset. The dataset we used is the fatigue-corrosion dataset from TomoBank [12]. This dataset consists of 25 distinct tomographic datasets of an aluminum alloy at various stages of fatigue cycles. Each dataset includes 1500 projection images of size 2560×2160 pixels, with the 1500 projections being equally distributed over $180°$. Additionally, ten dark fields and ten flat fields were captured before scanning and provided in each dataset.

For training and testing, we selected tomo_00056 with 14346 fatigue cycles and tomo_00055 with 14300 fatigue cycles. To create high-quality data, we performed flat-field correction using the median of all ten flat fields and dark fields. To produce corresponding low-quality data, we used one flat field and one dark field (randomly selected) for flat-field correction and selected 500 equally-spaced projection images out of the original 1500 projections. We reconstructed both low- and high-quality data using the GPU-accelerated FBP implementation of the AS-TRA toolbox [49]. Slight ring and zinger artifacts were still present, even after using the median flat fields and dark fields. Therefore, we applied additional processing steps for the high-quality data using TomoPy [17]: a median filter-based zinger removal algorithm on the projection images, and a polar coordinate-based ring removal algorithm on the reconstructed images. Parameters for these algorithms were chosen by visual assessment.

4.3 Implementation

The neural networks used in this work are the UNet network [40] and the mixed-scale dense (MS-D) network [36]. For our method, we used UNets with 4 intermediate channels and an MS-D network with a depth of 100 for every stage. The trainable parameters of the network used in each stage are shown in Table 2. As a comparison, we also trained UNet and MS-D networks as deep learning-based post-processing methods. Since our method consists of three stages with three separate neural networks, we increased the intermediate channels to 7 for UNet and depth to 180 for the MS-D network to make sure that the networks used in both approaches had a similar number of parameters, as shown in Table 2.

At each stage, the networks are trained for 200,

11

Table 2: Number of trainable parameters of used neural networks, both for our proposed method (total) and the deep learning-based post-processing method we compare with (post-proc.).

network	stage 1	stage 2	stage 3	total	post-proc.
UNet	122389	122425	122461	367275	373234
MS-D	45652	46553	47454	139659	146972

200, and 500 epochs with ADAM optimizer [24], L2 loss function, and initial learning rate of 10^{-3}. The training for the last stage was chosen to be longer than the first two stages because it had more complicated image features to learn in this stage. The deep learning-based post-processing networks were trained for 900 epochs to match the total epochs number. All training sessions used an early stopping strategy: if the validation loss was not improved for 10 successive epochs or the total training time exceeded 14 days, the training was stopped. The training data for the projection and reconstruction stage was augmented with horizontal flipping, vertical flipping, and rotation, while the training data for the sinogram stage was augmented with horizontal and vertical flipping only.

In this work, we used Peak Signal to Noise Ratio (PSNR) and Structural Similarity Index Measure (SSIM) as our performance metrics. These metrics were derived from high-quality reference data, and they facilitated the comparison of our method's performance with other techniques. Both PSNR and SSIM calculations were based on the reference data's range.

5 Results

5.1 Simulated data

We summarize the results on simulated data in three different aspects: (i) comparison of our method and deep learning-based post-processing; (ii) artifact reduction in each stage; (iii) impact of used neural networks in our method. We test various severity levels of Poisson noise, ring artifacts, and zinger artifacts by varying the corresponding parameters I_0, P_{ring}, and P_{zinger}. The figures shown in this section were

based on artifact levels $I_0 = 30$, $P_{\text{ring}} = 0.1$, and $P_{\text{zinger}} = 0.001$.

5.1.1 Comparison with post-processing

Figure 6 contrasts our multi-stage method with deep learning-based post-processing. Our multi-stage method yields images closer to the high-quality reference, effectively reducing ring and zinger artifacts unlike post-processing, which struggles with globally distributed ring artifacts. The difference also shows quantitatively in the PSNR and SSIM values: our method yields a PSNR of 22.25 dB and SSIM of 0.76, surpassing post-processing's PSNR of 19.89 dB and SSIM of 0.70. Table 3 details these comparisons for different artifact severities, with our method consistently outperforming in PSNR and SSIM metrics. Particularly when globally distributed artifacts and noise are present, our method shows significant improvement, emphasizing the effectiveness of processing across projection, sinogram, and reconstruction stages. These results show that globally distributed artifacts can be difficult to reduce with post-processing methods, but easy to reduce if processing also takes place in the projection and sinogram stage before reconstruction in the pipeline.

5.1.2 Artifact reduction in each stage

The impact of our multi-stage strategy on artifact reduction was evaluated by examining results at each stage, as shown in Figure 7. Initial projection image processing effectively reduced most zinger artifacts and some ring artifacts, with PSNR and SSIM improving to 18.17 dB and 0.45, respectively. Subsequent sinogram processing reduced most ring artifacts, though at the expense of some high-resolution details, further enhancing PSNR to 18.80 dB and
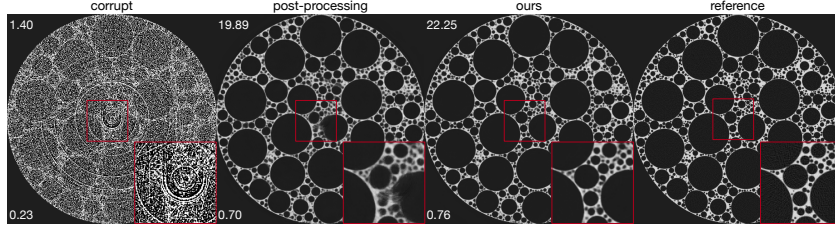
Figure 6: Results comparison of our method and deep learning-based post-processing. The red insets indicate enlarged views. The PSNR (top left) and SSIM (bottom left) are shown in each image.

Table 3: Comparison of our method with deep learning-based post-processing on the simulated foam phantom dataset, PSNRs and SSIMs are shown as the average of all slices, with best values shown in bold.

Parameters			PSNR/SSIM	
$(I_0, P_{\text{ring}}, P_{\text{zinger}})$	corrupt	method	UNet	MS-D
30, 0.1, 0.001	1.14/0.23	post-proc.	19.14/0.69	19.47/0.70
		our	20.92/0.74	**21.75/0.76**
100, 0.1, 0.001	4.07/0.27	post-proc.	21.18/0.73	21.98/0.75
		our	23.56/0.78	**24.50/0.79**
200, 0.1, 0.001	4.95/0.29	post-proc.	22.27/0.76	23.15/0.77
		our	25.00/0.79	**25.69/0.80**
100, 0, 0	8.47/0.35	post-proc.	24.16/0.78	24.14/0.78
		our	24.79/0.79	**25.59/0.80**
100, 0.2, 0	3.04/0.26	post-proc.	20.86/0.70	21.77/0.74
		our	22.96/0.77	**24.06/0.78**
100, 0.4, 0	0.70/0.23	post-proc.	20.01/0.71	21.02/0.73
		our	22.34/0.77	**23.48/0.78**
100, 0, 0.005	3.20/0.26	post-proc.	21.57/0.75	21.02/0.73
		our	**24.37/0.79**	23.65/0.78
100, 0, 0.01	0.90/0.23	post-proc.	20.18/0.73	20.97/0.73
		our	24.33/**0.79**	**24.86**/0.79

SSIM to 0.47. The final stage of processing the reconstructed images restored numerous image details, smoothed the image, and significantly elevated the PSNR to 22.25 dB and SSIM to 0.76.

5.1.3 Neural network architecture

Both UNet and MSD-Net effectively reduced artifacts in our method. However, it is worth noting that other image-to-image neural networks could also be suitable replacements for them. Additionally, different neural networks could be used for each stage of our method. Our results in Table 3 showed that MSD-Net achieved superior metrics in almost every case, for both our method and deep learning-based post-processing. MSD-Net's performance may be attributed to its lower number of trainable parameters compared to UNet. Specifically, the MSD-Net used for post-processing had only 47454 trainable parameters, while the UNet had 122461 trainable parameters. The low number trainable parameters of MSD-Net can help to reduce the risk of over-fitting in cases with a limited amount of training data [33].

5.2 Comparison with classical methods and deep learning

In this experiment, we compared classical methods followed by deep learning-based post-processing to our method using the foam phantom dataset with artifact level $I_0 = 100$, $P_{ring} = 0.1$, and $P_{zinger} = 0.001$. Five parameters needed determination for the classical methods. Using grid search, we tested various parameter combinations and calculated the MSE error for 3840 settings against reference projection data. Despite achieving the lowest MSE, the reconstructed image exhibited new artifacts around the rotation center. To address this issue, we visually assessed the reconstructed slices of processed data and selected a different combination of parameters. This new combination had slight ring artifacts but no severe additionally introduced artifacts. We show results for both combinations of parameters, with the specific parameter settings shown in Table 7 in the Appendix.

The data was processed by classical methods with the determined values and reconstructed using FBP.

Table 4: Comparison of the average PSNR and SSIM values of our proposed method with classical methods combined with deep learning-based post-processing on the simulated foam phantom dataset. The values are calculated as the average of all slices.

| method | PSNR/SSIM | |
	pre-processed	result
no artifact removal	4.07/0.27	-
grid	8.58/0.33	22.76/0.77
grid+visual	8.10/0.33	23.41/0.77
our	-	**24.50/0.79**

A 180-layer deep learning-based MS-D network was then trained. After training, both the classical methods and the trained MS-D network were applied to the test data. Results were contrasted with our multi-stage method, shown in Fig 8. These results indicate that artifacts from the initial setup persist after post-processing, affecting reduction performance. Our multi-stage method outperformed both classical and post-processing approaches, even with visually determined parameters for classical algorithms. Average metrics across slices are in Table 4. The results highlight the drawback of classical methods that parameters have to be set correctly to work properly, and choosing suboptimal values can result in additional artifacts. In contrast, our data-driven method requires no parameter tuning and outperforms classical methods combined with deep learning-based post-processing.

5.3 Cone-beam CT

To assess the effectiveness of our multi-stage method for cone-beam CT, we performed an experiment using the simulated foam phantom dataset. We simulated cone-beam CT with varying SODs on these phantoms and introduced fixed levels of artifacts ($I = 100$, $P_{ring} = 0.1$, and $P_{zinger} = 0.001$). Evaluation metrics were then computed for all test phantom reconstruction images and averaged. Parallel-beam reconstructed images served as our reference.

Table 5 demonstrates that our method effectively improved the PSNRs and SSIMs of the original cor-
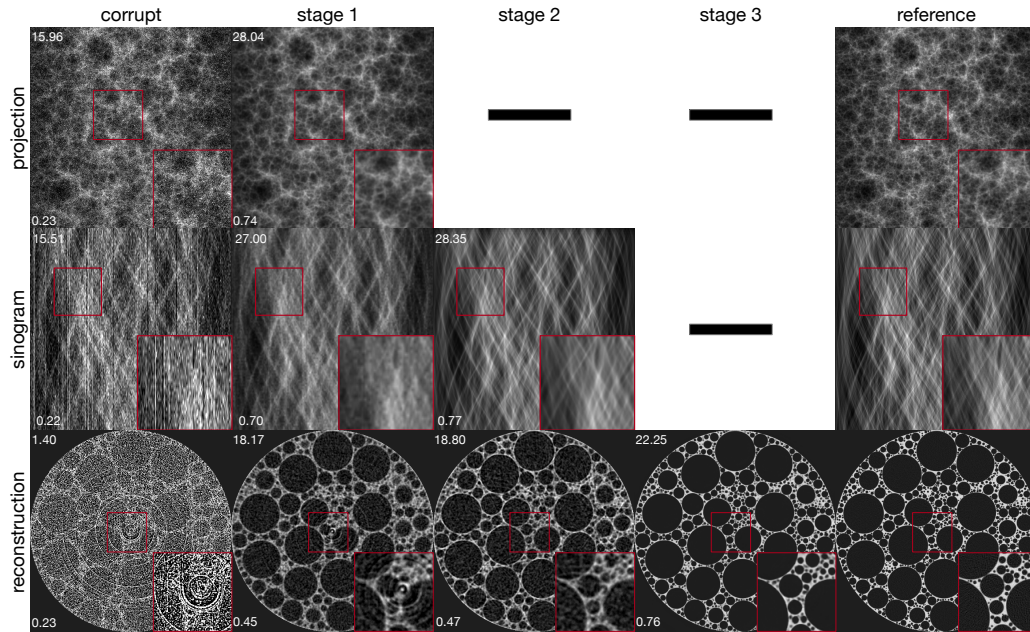
Figure 7: Method output of all three stages. The sinograms are cropped to squares for demonstration purposes. The red insets indicate enlarged views. The PSNR (top left) and SSIM (bottom left) are shown in each image.
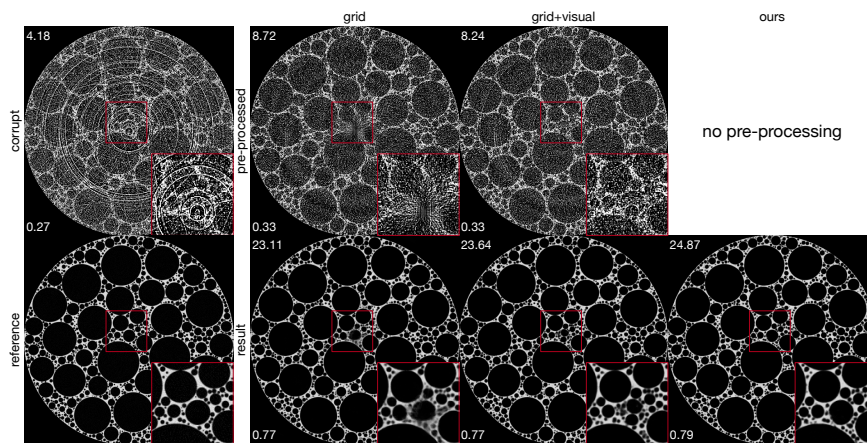
Figure 8: Results comparison of classical methods and our proposed method. The red insets indicate the enlarged views. PSNR and the SSIM are given in the top left and bottom left corners, respectively.

rupted data for all SODs. As the cone angle decreased, the PSNRs and SSIMs increased and approached the results obtained from parallel-beam reconstruction, indicating better artifact reduction performance. This experiment confirms that our method is applicable to cone-beam CT and achieves superior artifact reduction results, particularly as the cone angle decreases.

5.4   Real-world experimental data

The performance of our method on real-data data was similar to that on simulated data, as it was able to reduce artifacts effectively. Figure 9 shows the output of each stage in our method as well as deep learning-based post-processing as a comparison. The results show that the unprocessed corrupt reconstructed image includes severe ring, zinger, and noise artifacts. Similar to the simulated data, the first stage of processing reduced some ring and most zinger artifacts, while the ring and zinger artifacts were further reduced in the second stage. The final stage improved the image quality and reduced the remaining noise. As we compare our final stage output with deep learning-based post-processing, we can see that post-processing failed to reduce ring and zinger artifacts in this slice while our multi-stage method reduced them effectively.

The average PSNR and SSIM on all reconstructed slices are listed in Table 6. The results show that our method achieved better metrics than deep learning-based post-processing regardless of the used neural network architecture. Specifically, MS-D Net achieved better metrics than UNet using our method, but worse metrics than UNet in the post-processing setting. This result could be related to underfitting, as, even with a depth of 180, the trainable parameters of MS-D Net may still be too few on this dataset with 2560×2560 pixel images. MS-D Net achieved better metrics than UNet in our setting, indicating that our multi-stage strategy might require smaller networks than post-processing.

5.5   Computation time

We conducted a computational comparison between our method and post-processing using a simulated foam phantom with artifact levels $I_0 = 30$, $P_{ring} = 0.1$, and $P_{zinger} = 0.001$ using MS-D network. The raw corrupted projection consisted of 256 projection images of size 512×512 pixels. The computations were performed on a workstation equipped with an Intel i7-11700KF CPU and Nvidia RTX3070 GPU.

In our method, the raw projection underwent three sequential stages, with each stage involving a separate CNN. Additionally, the processed sinogram images were upsampled four times in the sinogram stage. As shown in Figure 10, the total inference time for our method was 56.18 seconds, while for post-processing it was 41.40 seconds. The training time for each stage of our multi-stage training was 9 minutes, 6 hours 50 minutes, and 3 hours 38 minutes, respectively. The total training time of our multi-stage training was 10 hours and 37 minutes. In contrast, the training time for post-processing was around 14 hours and 31 minutes.

6   Discussion

The experiments performed in this paper indicate that the proposed multi-stage method effectively reduces artifacts in CT images, outperforming classical methods combined with post-processing and deep learning-based post-processing. Our method achieves accurate artifact reduction on both the simulated and experimental datasets. In particular, our method demonstrates a greater advantage over post-processing when severe ring and zinger artifacts are present in the reconstructed images. However, even when only noise is present in the reconstructed images, our multi-stage strategy still outperforms post-processing. a qs Our method has several advantages over existing methods. First, it employs a multi-stage approach that reduces artifacts accurately in their natural domain, where the artifact is easier to reduce than in other domains. By processing data in the projection, sinogram, and reconstruction domains, our method can effectively reduce different artifacts

Table 5: Results of our method on cone-beam CT images. PSNR and SSIM are shown in the table.

cone angle (°)	22.62	11.42	7.62	5.72	4.58	3.82	0
			PSNR/SSIM				
corrupt	5.66/0.28	5.73/0.29	5.70/0.29	5.66/0.29	5.62/0.29	5.60/0.29	4.07/0.27
ours	19.55/0.63	22.07/0/73	22.85/0.75	23.41/0.76	23.45/0.77	23.53/0.77	24.50/0.79
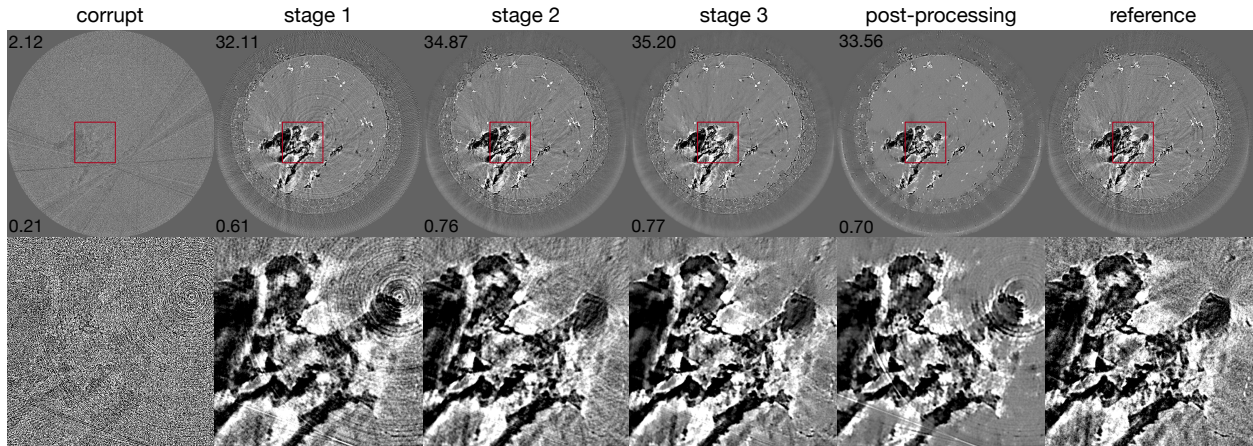
Figure 9: Results comparison of our method and deep learning-based post-processing on `fatigue-corrosion` datasets. The output of all three stages of our method is shown. The red insets indicate enlarged views. The PSNR (top left) and SSIM (bottom left) with respect to the reference image are shown in the image.

Table 6: Comparison of our method with deep learning-based post-processing on an experimental dataset.

method	network	PSNR	SSIM
unprocessed	n/a	6.22	0.21
post-proc.	UNet	36.70	0.80
our		36.85	0.80
post-proc.	MS-D	36.04	0.78
our		**37.13**	**0.82**
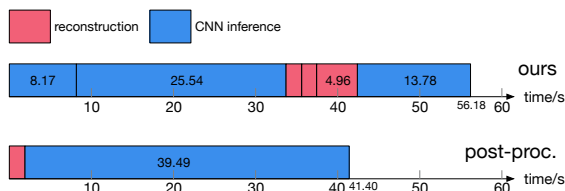
Figure 10: Comparison of inference time between our method and post-processing. Our method involves reconstructing the raw projection, the processed projection, and the processed sinogram, requiring three passes through CNNs at each stage. In contrast, post-processing only involves reconstructing the raw projection and applying it to the image domain CNN.

jointly. Second, the neural networks in each stage can be selected and trained independently to optimize performance for specific artifacts, enabling computationally efficient training. Third, our method can be easily integrated into existing CT pipelines without reducing the throughput of pipelines. Overall, our method provides an efficient and effective solution for reducing artifacts in CT images.

Although high-quality reference data can be acquired in various manners as explained, such as scanning with high-dose CT, using more sophisticated reconstruction methods, or additional post-processing steps, our proposed method still relies on these extra steps to obtain high-quality reference data. These steps may require additional time and effort in real-world scenarios. Therefore, it is worth exploring the integration of our multi-stage strategy with self-supervised methods, for example by applying Noise2Inverse [19] in a multi-stage manner. This could potentially reduce the reliance on high-quality reference data and improve the applicability of our method in real-world scenarios.

In principle, the proposed method for artifact reduction could be extended to other computational imaging modalities with similar processing pipelines. In many settings, reconstructed images are computed through a series of processing steps in different domains, with artifacts in the measurements propagating through the pipeline resulting in artifacts in the reconstructed images. The key idea of applying deep learning within the pipeline instead of only at the end of the pipeline could be beneficial to improve the image quality of other imaging modalities, e.g. magnetic resonance imaging (MRI) or positron emission tomography (PET). By incorporating our multi-stage strategy into these modalities, artifact reduction can be achieved in their natural domain, potentially leading to improved image quality.

7 Conclusion

In this work, we present a novel multi-stage artifact reduction method for CT images. Our approach involves three stages, each targeting a different type of image artifact in its corresponding domain: pro-

jection, sinogram, and reconstruction. We employ three separate neural networks, one for each stage, to jointly reduce artifacts in their respective domains. The networks are trained independently from each other in a sequential manner, ensuring computationally efficient training. Our experimental results demonstrate that our method outperforms deep learning-based post-processing techniques in terms of artifact reduction accuracy, both for simulated data and real-world experimental data. Furthermore, our approach is applicable to both parallel- and cone-beam CT, making it a versatile tool that can be integrated into existing CT pipelines to improve image quality.

Acknowledgments

Appendix

Table 7 includes the chosen parameters of classical artifact reduction methods.

References

[1] J. Adler and O. Öktem. Solving ill-posed inverse problems using iterative deep neural networks. *Inverse Problems*, 33(12):124007, 2017.

[2] J. Adler and O. Öktem. Learned primal-dual reconstruction. *IEEE transactions on medical imaging*, 37(6):1322–1332, 2018.

[3] E. M. A. Anas, J. Kim, S. Y. Lee, and M. K. Hasan. Ring artifact corrections in flat-panel detector based cone beam ct. In *Medical Imaging 2011: Physics of Medical Imaging*, volume 7961, pages 799–808. SPIE, 2011.

[4] E. M. A. Anas, S. Y. Lee, and M. K. Hasan. Removal of ring artifacts in ct imaging through detection and correction of stripes in the sinogram.

[5] F. E. Boas, D. Fleischmann, et al. Ct artifacts: causes and reduction techniques. *Imaging Med*, 4(2):229–240, 2012.

[6] M. Boin and A. Haibel. Compensation of ring artefacts in synchrotron tomographic images. *Optics express*, 14(25):12071–12075, 2006.

[7] Z. Chao and H.-J. Kim. Removal of computed tomography ring artifacts via radial basis function artificial neural networks. *Physics in Medicine & Biology*, 64(23):235015, 2019.

[8] H. Chen, Y. Zhang, W. Zhang, P. Liao, K. Li, J. Zhou, and G. Wang. Low-dose ct via convolutional neural network. *Biomedical optics express*, 8(2):679–694, 2017.

[9] Y. Chen, L. Shi, Q. Feng, J. Yang, H. Shu, L. Luo, J.-L. Coatrieux, and W. Chen. Artifact suppressed dictionary learning for low-dose ct image processing. *IEEE transactions on medical imaging*, 33(12):2271–2292, 2014.

[10] L. C. Croton, G. Ruben, K. S. Morgan, D. M. Paganin, and M. J. Kitchen. Ring artifact suppression in x-ray computed tomography using a simple, pixel-wise response correction. *Optics express*, 27(10):14231–14245, 2019.

[11] K. Dabov, A. Foi, V. Katkovnik, and K. Egiazarian. Image denoising by sparse 3-d transform-domain collaborative filtering. *IEEE Transactions on image processing*, 16(8):2080–2095, 2007.

[12] F. De Carlo, D. Gürsoy, D. J. Ching, K. J. Batenburg, W. Ludwig, L. Mancini, F. Marone, R. Mokso, D. M. Pelt, J. Sijbers, et al. Tomobank: a tomographic data repository for computational x-ray science. *Measurement Science and Technology*, 29(3):034004, 2018.

[13] T. Faragó, S. Gasilov, I. Emslie, M. Zuber, L. Helfen, M. Vogelgesang, and T. Baumbach.

[4] ... *Physics in Medicine & Biology*, 55(22):6911, 2010.

Table 7: Determined parameters of classical methods: (i) the expected difference value between the outlier value and the median value of the image (dif), (ii) the median filter size (size) for outlier removal function, (iii) the discrete wavelet transform levels (level), (iv) the type of wavelet filter (type), and (v) the damping parameter in Fourier space (sigma).

approach	(i) dif	(ii) size	(iii) level	(iv) wname	(v) sigma
grid	0.5	3	4	sym5	8
grid+visual	0.5	3	4	sym5	1
scipy+grid	3.56×10^{-6}	3	4	sym5	2

Tofu: a fast, versatile and user-friendly image processing toolkit for computed tomography. *Journal of Synchrotron Radiation*, 29(3), 2022.

[14] M. U. Ghani and W. C. Karl. Deep learning-based sinogram completion for low-dose ct. In *2018 IEEE 13th Image, Video, and Multidimensional Signal Processing Workshop (IVMSP)*, pages 1–5. IEEE, 2018.

[15] M. U. Ghani and W. C. Karl. Fast enhanced ct metal artifact reduction using data domain deep learning. *IEEE Transactions on Computational Imaging*, 6:181–193, 2019.

[16] J. C. R. Giraldo, Z. S. Kelm, L. S. Guimaraes, L. Yu, J. G. Fletcher, B. J. Erickson, and C. H. McCollough. Comparative study of two image space noise reduction methods for computed tomography: bilateral filter and nonlocal means. In *2009 Annual International Conference of the IEEE Engineering in Medicine and Biology Society*, pages 3529–3532. IEEE, 2009.

[17] D. Gürsoy, F. De Carlo, X. Xiao, and C. Jacobsen. Tomopy: a framework for the analysis of synchrotron tomographic data. *Journal of synchrotron radiation*, 21(5):1188–1193, 2014.

[18] P. C. Hansen, J. Jørgensen, and W. R. Lionheart. *Computed Tomography: Algorithms, Insight, and Just Enough Theory*. SIAM, 2021.

[19] A. A. Hendriksen, D. M. Pelt, and K. J. Batenburg. Noise2inverse: Self-supervised deep convolutional denoising for tomography. *IEEE Trans-*

actions on Computational Imaging, 6:1320–1335, 2020.

[20] K. H. Jin, M. T. McCann, E. Froustey, and M. Unser. Deep convolutional neural network for inverse problems in imaging. *IEEE Transactions on Image Processing*, 26(9):4509–4522, 2017.

[21] M. Kachelriess, O. Watzke, and W. A. Kalender. Generalized multi-dimensional adaptive filtering for conventional and spiral single-slice, multi-slice, and cone-beam ct. *Medical physics*, 28(4):475–490, 2001.

[22] D. Kazantsev, F. Bleichrodt, T. van Leeuwen, A. Kaestner, P. J. Withers, K. J. Batenburg, and P. D. Lee. A novel tomographic reconstruction method based on the robust student's t function for suppressing data outliers. *IEEE Transactions on Computational Imaging*, 3(4):682–693, 2017.

[23] R. A. Ketcham. New algorithms for ring artifact removal. In *Developments in X-ray tomography V*, volume 6318, pages 216–222. SPIE, 2006.

[24] D. P. Kingma and J. Ba. Adam: A method for stochastic optimization. In Y. Bengio and Y. LeCun, editors, *3rd International Conference on Learning Representations, ICLR 2015, San Diego, CA, USA, May 7-9, 2015, Conference Track Proceedings*, 2015.

[25] H. Lee, C. Huang, S. Yune, S. H. Tajmir, M. Kim, and S. Do. Machine friendly machine

learning: interpretation of computed tomography without image reconstruction. *Scientific reports*, 9(1):1–9, 2019.

[26] J. Leuschner, M. Schmidt, P. S. Ganguly, V. Andriiashen, S. B. Coban, A. Denker, D. Bauer, A. Hadjifaradji, K. J. Batenburg, P. Maass, et al. Quantitative comparison of deep learning-based image reconstruction methods for low-dose and sparse-angle ct applications. *Journal of Imaging*, 7(3):44, 2021.

[27] Y. Liu, J. Ma, Y. Fan, and Z. Liang. Adaptive-weighted total variation minimization for sparse data toward low-dose x-ray computed tomography image reconstruction. *Physics in Medicine & Biology*, 57(23):7923, 2012.

[28] Y. Mäkinen, S. Marchesini, and A. Foi. Ring artifact reduction via multiscale nonlocal collaborative filtering of spatially correlated noise. *Journal of synchrotron radiation*, 28(3), 2021.

[29] J. Mertens, J. Williams, and N. Chawla. A method for zinger artifact reduction in high-energy x-ray computed tomography. *Nuclear Instruments and Methods in Physics Research Section A: Accelerators, Spectrometers, Detectors and Associated Equipment*, 800:82–92, 2015.

[30] K. A. Mohan, S. Venkatakrishnan, L. F. Drummy, J. Simmons, D. Y. Parkinson, and C. A. Bouman. Model-based iterative reconstruction for synchrotron x-ray tomography. In *2014 IEEE International Conference on Acoustics, Speech and Signal Processing (ICASSP)*, pages 6909–6913. IEEE, 2014.

[31] B. Münch, P. Trtik, F. Marone, and M. Stampanoni. Stripe and ring artifact removal with combined wavelet—fourier filtering. *Optics express*, 17(10):8567–8591, 2009.

[32] P. Paleo and A. Mirone. Ring artifacts correction in compressed sensing tomographic reconstruction. *Journal of synchrotron radiation*, 22(5):1268–1278, 2015.

[33] D. M. Pelt, K. J. Batenburg, and J. A. Sethian. Improving tomographic reconstruction from limited data using mixed-scale dense convolutional neural networks. *Journal of Imaging*, 4(11):128, 2018.

[34] D. M. Pelt, A. A. Hendriksen, and K. J. Batenburg. Foam-like phantoms for comparing tomography algorithms. *Journal of Synchrotron Radiation*, 29(1), 2022.

[35] D. M. Pelt and D. Y. Parkinson. Ring artifact reduction in synchrotron x-ray tomography through helical acquisition. *Measurement Science and Technology*, 29(3):034002, 2018.

[36] D. M. Pelt and J. A. Sethian. A mixed-scale dense convolutional neural network for image analysis. *Proceedings of the National Academy of Sciences*, 115(2):254–259, 2018.

[37] M. Persson, D. Bone, and H. Elmqvist. Total variation norm for three-dimensional iterative reconstruction in limited view angle tomography. *Physics in Medicine & Biology*, 46(3):853, 2001.

[38] L. Ritschl, F. Bergner, C. Fleischmann, and M. Kachelrieß. Improved total variation-based ct image reconstruction applied to clinical data. *Physics in Medicine & Biology*, 56(6):1545, 2011.

[39] M. Rivers. Tutorial introduction to x-ray computed microtomography data processing. *University of Chicago*, 1998.

[40] O. Ronneberger, P. Fischer, and T. Brox. U-net: Convolutional networks for biomedical image segmentation. In *International Conference on Medical image computing and computer-assisted intervention*, pages 234–241. Springer, 2015.

[41] L. I. Rudin, S. Osher, and E. Fatemi. Nonlinear total variation based noise removal algorithms. *Physica D: nonlinear phenomena*, 60(1-4):259–268, 1992.

[42] M. Salehjahromi, Q. Wang, Y. Zhang, L. A. Gjesteby, D. Harrison, G. Wang, P. M. Edic, and

H. Yu. A new iterative algorithm for ring artifact reduction in ct using ring total variation. *Medical physics*, 46(11):4803–4815, 2019.

[43] E. Y. Sidky, C.-M. Kao, and X. Pan. Accurate image reconstruction from few-views and limited-angle data in divergent-beam ct. *Journal of X-ray Science and Technology*, 14(2):119–139, 2006.

[44] J. Sijbers and A. Postnov. Reduction of ring artefacts in high resolution micro-ct reconstructions. *Physics in Medicine & Biology*, 49(14):N247, 2004.

[45] E. A. Smith, J. R. Dillman, M. M. Goodsitt, E. G. Christodoulou, N. Keshavarzi, and P. J. Strouse. Model-based iterative reconstruction: effect on patient radiation dose and image quality in pediatric body ct. *Radiology*, 270(2):526, 2014.

[46] S. Titarenko, P. J. Withers, and A. Yagola. An analytical formula for ring artefact suppression in x-ray tomography. *Applied Mathematics Letters*, 23(12):1489–1495, 2010.

[47] V. Titarenko. Analytical formula for two-dimensional ring artefact suppression. *Journal of synchrotron radiation*, 23(6):1447–1461, 2016.

[48] W. Vågberg, J. C. Larsson, and H. M. Hertz. Removal of ring artifacts in microtomography by characterization of scintillator variations. *Optics Express*, 25(19):23191–23198, 2017.

[49] W. Van Aarle, W. J. Palenstijn, J. De Beenhouwer, T. Altantzis, S. Bals, K. J. Batenburg, and J. Sijbers. The astra toolbox: A platform for advanced algorithm development in electron tomography. *Ultramicroscopy*, 157:35–47, 2015.

[50] N. T. Vo, R. C. Atwood, and M. Drakopoulos. Superior techniques for eliminating ring artifacts in x-ray micro-tomography. *Optics express*, 26(22):28396–28412, 2018.

[51] J. Wang, H. Lu, T. Li, and Z. Liang. Sinogram noise reduction for low-dose ct by statistics-based nonlinear filters. In *Medical Imaging 2005: Image Processing*, volume 5747, pages 2058–2066. SPIE, 2005.

[52] Z. Wang, J. Li, and M. Enoh. Removing ring artifacts in cbct images via generative adversarial networks with unidirectional relative total variation loss. *Neural Computing and Applications*, 31(9):5147–5158, 2019.

[53] Q. Xu, H. Yu, X. Mou, L. Zhang, J. Hsieh, and G. Wang. Low-dose x-ray ct reconstruction via dictionary learning. *IEEE transactions on medical imaging*, 31(9):1682–1697, 2012.

[54] Q. Yang, P. Yan, Y. Zhang, H. Yu, Y. Shi, X. Mou, M. K. Kalra, Y. Zhang, L. Sun, and G. Wang. Low-dose ct image denoising using a generative adversarial network with wasserstein distance and perceptual loss. *IEEE transactions on medical imaging*, 37(6):1348–1357, 2018.

[55] H. Yu and G. Wang. Compressed sensing based interior tomography. *Physics in medicine & biology*, 54(9):2791, 2009.

[56] H. Yuan, J. Jia, and Z. Zhu. Sipid: A deep learning framework for sinogram interpolation and image denoising in low-dose ct reconstruction. In *2018 IEEE 15th International Symposium on Biomedical Imaging (ISBI 2018)*, pages 1521–1524. IEEE, 2018.

[57] L. Yuan, Q. Xu, B. Liu, Z. Wang, S. Liu, C. Wei, and L. Wei. A deep learning-based ring artifact correction method for x-ray ct. *Radiation Detection Technology and Methods*, pages 1–11, 2021.

[58] Y. Zhu, M. Zhao, H. Li, and P. Zhang. Micro-ct artifacts reduction based on detector random shifting and fast data inpainting. *Medical physics*, 40(3):031114, 2013.